Supporting Information

Heterojunction cobalt-iron fluorides deposited on MXene for enhanced oxygen evolution reaction

Qiaowei Wang[a,b,c], Qiongdan Xie[a,b], Shuli Wang[c] and Ligang Feng[c*]

[a] School of New Energy and intelligent Networked Automobile, Sanya University, Sanya, 572018, PR China. E-mail: qiaoweiwang@sanyau.edu.cn

[b] New Energy and Intelligent Vehicle Engineering Research Center of Hainan Province Sanya, 572018, PR China.

[c] School of Chemistry and Chemical Engineering, Yangzhou University, Yangzhou 225002, P.R. China. E-mail: ligang.feng@kust.edu.cn, fenglg11@gmail.com

1. Experimental Section

1.1 Materials

Cobalt nitrate hexahydrate ($Co(NO_3)_2 \cdot 6H_2O$), Iron nitrate nonahydrate ($Fe(NO_3)_3 \cdot 9H_2O$), Ammonium fluoride (NH_4F), Urea (CH_4N_2O), Ti_3AlC_2 (MAX), dicyanodiamide Nafion (5wt%) were purchased from Sigma-Aldrich. Ethanol was purchased from Sinopharm Chemical Reagent Beijing Co. LTD. All chemicals used were of analytical grade and used without further purification in this study. All solutions were prepared with ultrapure water with a resistance of 18.2 MΩ (Thermo Fisher Scientific Co. LTD, USA).

1.2 Synthesis of the catalysts

1.2.1 Synthesis of $Ti_3C_2T_x$ MXene

$Ti_3C_2T_x$ MXene was fabricated by etching of Ti_3AlC_2 (MAX) powder. In general, Ti_3AlC_2 powder (2 g) was slowly added to a 40 % HF solution (30 mL) and stirred for 24 h at room temperature. The resulting product was centrifuged at 3000 rpm for 5 minutes and washed several times with deionized water. Finally, the as-formed product was dried in a vacuum oven at 60 ℃ for 12 h to obtain the $Ti_3C_2T_x$ MXene.

1.2.2 Synthesis of Cobalt-Iron Precursor/MXene

Cobalt-iron precursor /MXene was prepared by the oil bath method. First, 1.66 g $Co(NO_3)_2$ $6H_2O$, 2.81g $Fe(NO_3)_3$ $9H_2O$, 0.42 g NH_4F, and 1.71 g urea were added to a beaker. Then add 40 ml of deionized water, stir for 10min under the condition of magnetic stirring, then add 0.1 g of MXene, and sonicate for 45 min to form a homogeneous solution. The mixture was then transferred to a three-necked flask, and a condensing reflux unit was set up and finally heated for 6 hours with stirring in an oil bath at 150 ℃. When the suspension cools naturally to room temperature, it is washed several times with ultrapure water by filtration. The product is collected and dried overnight in a vacuum drying oven at 60 ℃.

1.2.3 Synthesis of Co(OH)F/MXene

Co(OH)F/MXene was prepared by the oil bath method. First, 1.66 g $Co(NO_3)_2$ $6H_2O$, 0.42 g NH_4F, and 1.71 g urea were added to a beaker. Then add 40ml of deionized water, stir for 10 min under the condition of magnetic stirring, then add 0.1 g of MXene, and sonicate for 45 min to form a homogeneous solution. The mixture was then transferred to a three-necked flask, and a condensing reflux unit was set up and finally heated for 6 hours with stirring in an oil bath at 150 ℃. When the suspension cools naturally to room temperature, it is washed several times with ultrapure water by filtration. The product is collected and dried overnight in a vacuum drying oven at 60 ℃.

1.2.4 Synthesis of iron precursor/MXene

Iron precursor/MXene was prepared by the oil bath method. First, 2.81g $Fe(NO_3)_3$ $9H_2O$, 0.42 g NH_4F, and 1.71 g urea were added to a beaker. Then add 40 ml of deionized water, stir for 10min under the condition of magnetic stirring, then add 0.1 g of MXene, and sonicate for 45 min to form a homogeneous solution. The mixture was then transferred to a three-necked flask, and a condensing reflux unit was set up and finally heated for 6 hours with stirring in an oil bath at 150 ℃. When the

suspension cools naturally to room temperature, it is washed several times with ultrapure water by filtration. The product is collected and dried overnight in a vacuum drying oven at 60 ℃.

1.2.5 Synthesis of CoF_2/FeF_2@MXene

The obtained Cobalt-iron precursor/MXene was prepared in a tube furnace for low-temperature fluoridation etching treatment. The Cobalt-iron precursor/MXene and ammonium fluoride (NH_4F) were placed at two separate positions of a porcelain boat with a mass ratio of 1:10 (w/w) in the furnace in a nitrogen gas atmosphere at 400 ℃ for 2 h. The resulting product was thoroughly washed with deionized water and ethanol and then dried in a vacuum oven at 60 ℃ for 12 h.

1.2.6 Synthesis of CoF_2/MXene

The obtained Co(OH)F/MXene was prepared in a tube furnace for low-temperature fluoridation etching treatment. The Co(OH)F/MXene and ammonium fluoride (NH_4F) were placed at two separate positions of a porcelain boat with a mass ratio of 1:10 (w/w) in the furnace in a nitrogen gas atmosphere at 350 ℃ for 2 h. The resulting product was thoroughly washed with deionized water and ethanol and then dried in a vacuum oven at 60 ℃ for 12 h.

1.2.7 Synthesis of FeF_2/MXene

The obtained iron precursor/MXene was prepared in a tube furnace for low-temperature fluoridation etching treatment. The iron precursor/MXene and ammonium fluoride (NH_4F) were placed at two separate positions of a porcelain boat with a mass ratio of 1:10 (w/w) in the furnace in a nitrogen gas atmosphere at 450 ℃ for 2 h. The resulting product was thoroughly washed with deionized water and ethanol and then dried in a vacuum oven at 60 ℃ for 12 h.

It is important to clarify that NH_4F was introduced during the precursor preparation step primarily as a morphology-directing and structure-regulating agent, rather than as the main source of fluorine in the final product. The fluorine in the crystalline CoF_2/FeF_2 active phase originates predominantly from the low-temperature fluoridation etching process since without this step, the fluoride can not be obtained.

In the precursor synthesis, the F-ions coordinate with metal ions and modulate crystallization kinetics, facilitating the formation of a well-structured metal hydroxyfluoride precursor with defined nanosheet morphology. If NH_4F were omitted, the absence of such regulation would lead to rapid and disordered precipitation, resulting in the formation of bulky oxide/hydroxide aggregates with significantly reduced specific surface area and limited exposure of active sites. Therefore, while NH_4F in the precursor step is indispensable for constructing the optimal intermediate morphology, the fluorine atoms constituting the final active fluoride phase are incorporated mainly during the subsequent fluoridation etching step.

Noted that the temperature selection was based on the distinct fluorination behaviors of the cobalt and iron precursors. The cobalt-based precursor undergoes fluorination readily at relatively low temperatures, while excessively high temperatures may lead to over-crystallization or partial decomposition of CoF_2. In contrast, the iron precursor requires a higher temperature to complete the fluorination reaction and form FeF_2, due to the higher bond formation energy of Fe-F, which

demands stronger thermal driving force. For the bimetallic cobalt-iron precursor, an intermediate temperature of 400 °C was chosen to facilitate the simultaneous formation of CoF_2 and FeF_2, promoting the construction of a heterojunction structure while avoiding excessive crystallization or decomposition of either component[1-3].

2. Physical characterizations

Powder X-ray diffraction (XRD) patterns were recorded on a Bruker D8 Advance powder X-ray diffractometer using a Cu K_α (λ = 1.5405 Å) radiation source operating at 40 kV and 30 mA at a scanning rate of 5° min^{-1}. The morphology and microstructure of the product were analyzed by scanning electron microscope (SEM, S4800II) and transmission electron microscopy (TEM, Philips, Tecnai 12 F30 S-TWIN). High-resolution TEM (HRTEM) was conducted on a TECNAI G2 operating at 200 kV. X-ray photoelectron spectroscopy (XPS) measurements were carried out on an ESCALAB250Xi spectrometer with an Al K_α radiation source.

3. Electrochemical measurements

All the electrochemical measurements were tested in a typical three-electrode system linked to a Bio-Logic SAS analyzer (France). Our catalyst electrode served as the working electrode with a graphite rod as the counter electrode; a mercury/mercury oxide electrode (Hg/HgO) as the reference electrode was employed through a double salt bridge and lugging capillary, and it was calibrated before and after the experiments to ensure the accuracy. A glassy carbon electrode (GCE, 3.0 mm diameter) was used to support the catalysts. The working electrode was prepared as follows: 5 mg of catalyst was dispersed entirely into the mixture of 50 μL Nafion and 950 μL ethanol, and ultrasonicated for 30 min to form a uniform catalyst suspension. Then, 10 μL of the catalyst suspension was loaded dropwise onto the GCE. The prepared working electrode was placed in 1 M KOH and treated with N_2 for electrochemical testing. All the potentials used were converted into RHE: ($E_{(RHE)} = E_{(Hg/HgO)} + 0.0591*pH + 0.098$ V). The catalytic performance of the samples for OER was evaluated by linear scan voltammetry (LSV), and the scanning rate was 5 mV s^{-1}.

The electrochemical impedance spectroscopy (EIS) frequency range was 1000 kHz ~ 0.01Hz. The chronoamperometry (CA) was measured at a constant potential of 1.48 V vs RHE for 30 h. All tests were carried out at room temperature (around 25 °C), and all LSV curves were corrected without iR compensation.

To estimate the effective surface areas of catalysts, we measured the double-layer capacitance (C_{dl}) by the cyclic voltammetry (CV) method by varying the scan rate (20, 40, 60, 80, and 100 mV s^{-1}) in the non-Faradaic region from 0.89 to 0.99 V vs RHE. By plotting $\Delta j = 1/2 (j_{anodic} - j_{cathodic})$ at the middle potential (0.94 V) against the scanning rates, the linear slope is C_{dl}. j_{anodic} and $j_{cathodic}$ are anodic and cathodic current densities at the anode (>0) and cathode (<0), respectively. The electrochemically active surface area (ECSA) was achieved by normalizing the C_{dl} to a standard-

specific capacitance. ECSA was calculated according to the following equations S1, 40 μF cm^{-2} was adopted as the specific capacitance (C_s) value, as regards previous reports [4, 5], and S is the surface area of the electrode (here is 0.07 cm^{-2}):

Equation S1: $$ECSA = \frac{C_{dl} * S}{C_s}$$

The turnover frequency (TOF) values were calculated from the equation S2:

Equation S2: $$TOF = \frac{j * S}{4 * F * m}$$

Where *j* is the current density at a specific potential, F is the Faraday constant (96485 C mol^{-1}) and m is the number of moles of active materials.

4. Density functional theory (DFT) calculation

DFT calculations were performed using the CASTEP module of the Materials Studio software (Accelrys Inc.). The generalized gradient approximation method (GGA) with the Perdew-Burke-Ernzerhof (PBE) functional was used to describe the exchange and correlation interactions [6, 7]. The interactions between valence electrons and ionic cores were described by Ultrasoft pseudo-potential and dispersion adjustment using DFT-D correction. The electronic wave functions were expanded on a plane wave basis with a cut-off energy of 380 eV, and the self-consistent field (SCF) tolerance is 1.0×10^{-6} eV/atom. The optimization is completed when the energy, maximum force, maximum stress, and maximum displacement are less than 5.0×10^{-6} eV/atom, 0.01 eV/Å, 0.02 GPa, and 5.0×10^{-4} Å, respectively. A vacuum slab with a thickness greater than 15 Å was used in the z-direction. The Gibbs free energy of the reaction and the Gibbs free energy of the adsorption intermediate can be obtained from equation S3 [8]:

Equation S3: $\Delta G = \Delta E + \Delta ZPE - T\Delta S$

where ΔE is the energy of the reaction, ZPE is the zero-point energy change, and ΔS is the entropy change.

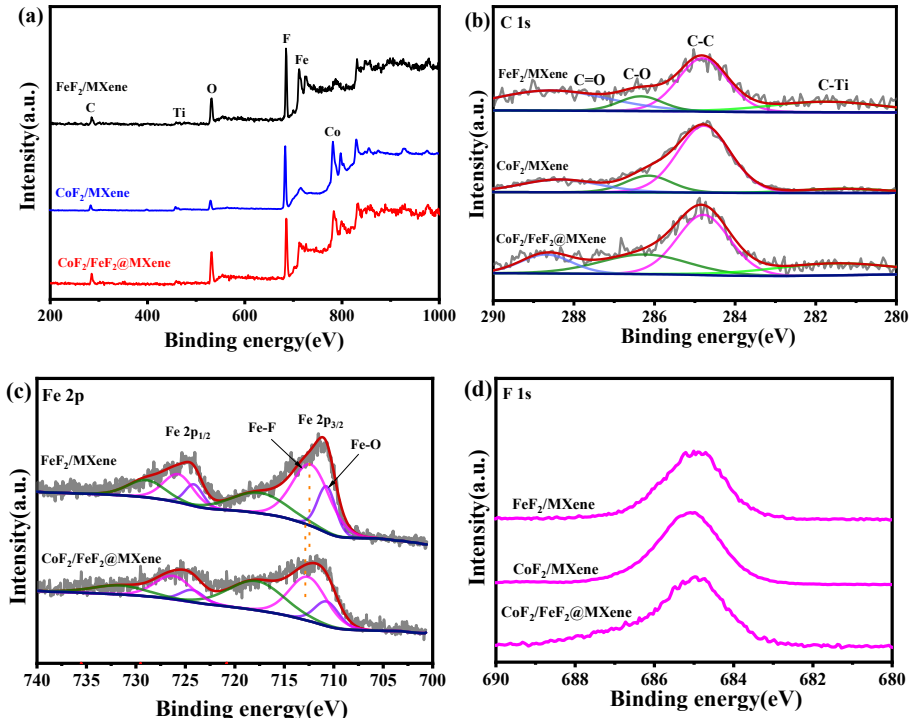

Fig. S1. (a) The XPS survey spectra; High-resolution XPS spectrum for (b) C 1s of FeF_2/MXene, CoF_2/MXene and CoF_2/FeF_2@MXene; (c) Fe 2p of FeF_2/MXene and CoF_2/FeF_2@MXene (d) F 1s of FeF_2/MXene, CoF_2/MXene and CoF_2/FeF_2@MXene FeF_2/MXene, CoF_2/MXene and CoF_2/FeF_2@MXene.

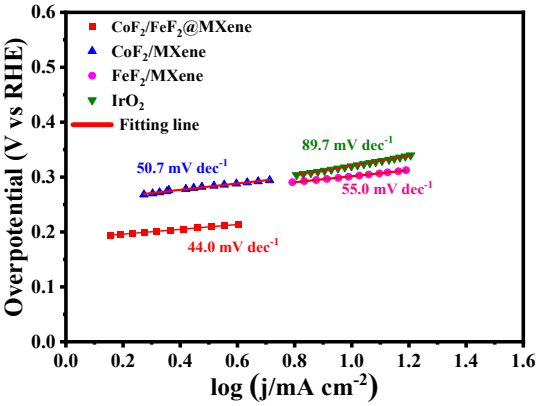

Fig. S2. Corresponding OER Tafel plots.

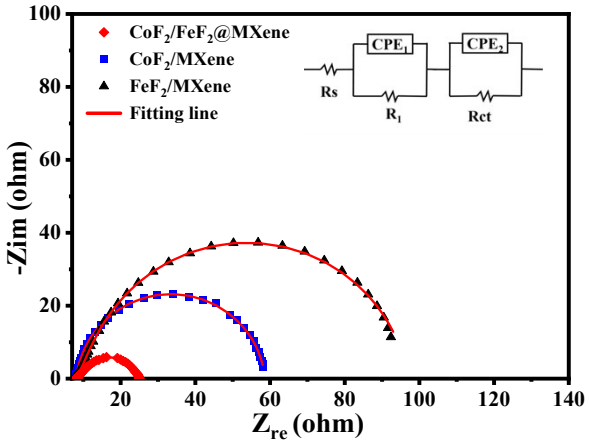

Fig. S3. Nyquist plots of the CoF_2/FeF_2@MXene, CoF_2/MXene and FeF_2/MXene.

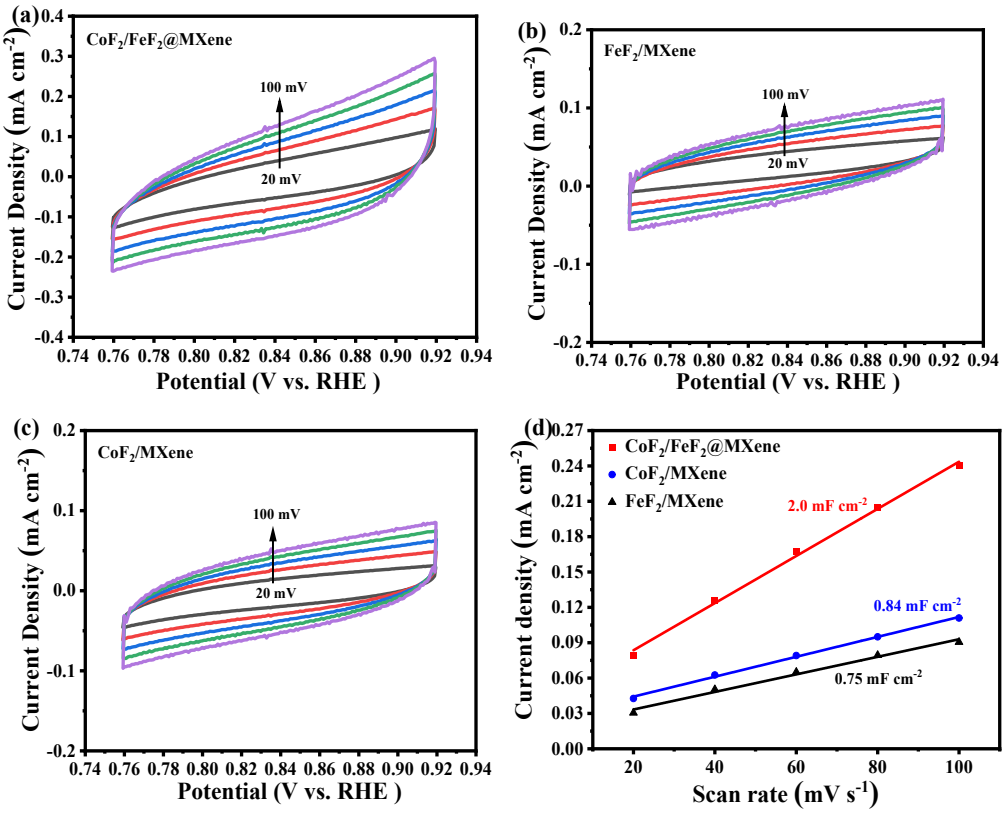

Fig. S4. CV curves of (a) CoF_2/FeF_2@MXene, (b) FeF_2/MXene and (c)CoF_2/MXene samples in the non-faradaic capacitance current range from 0.75 V to 0.91 V (vs RHE) at scan rates of 20, 40, 60, 80 and 100 mV s^{-1}. (d) The C_{dl} values of CoF_2/FeF_2@MXene, CoF_2/MXene and FeF_2/MXene samples.

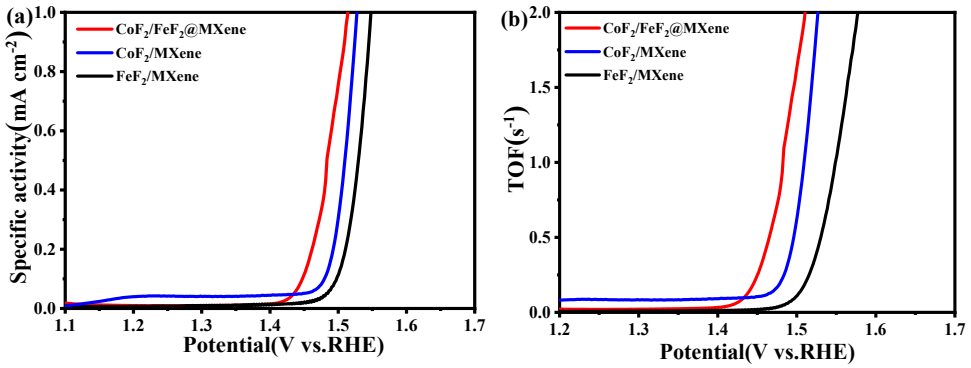

Fig. S5. (a) The specific activity of CoF_2/FeF_2@MXene, CoF_2/MXene and FeF_2/MXene. (b) TOF curves of CoF_2/FeF_2@MXene, CoF_2/MXene and FeF_2/MXene.

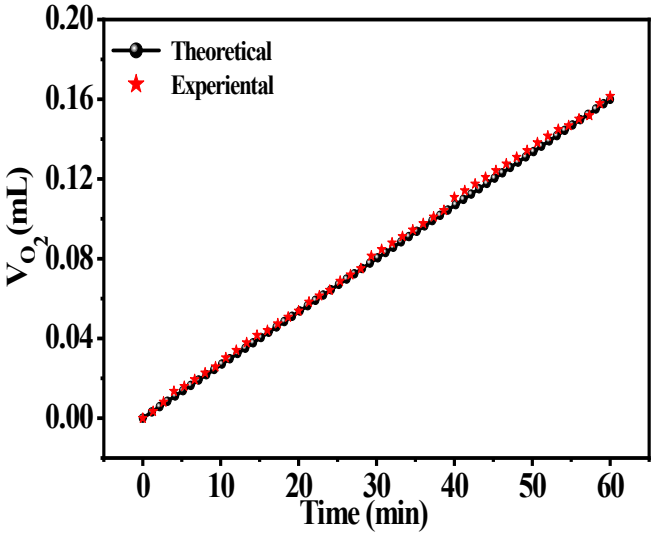

Fig. S6 The Faradaic efficiency curve of CoF_2/FeF_2@MXene in 1 M KOH solution.

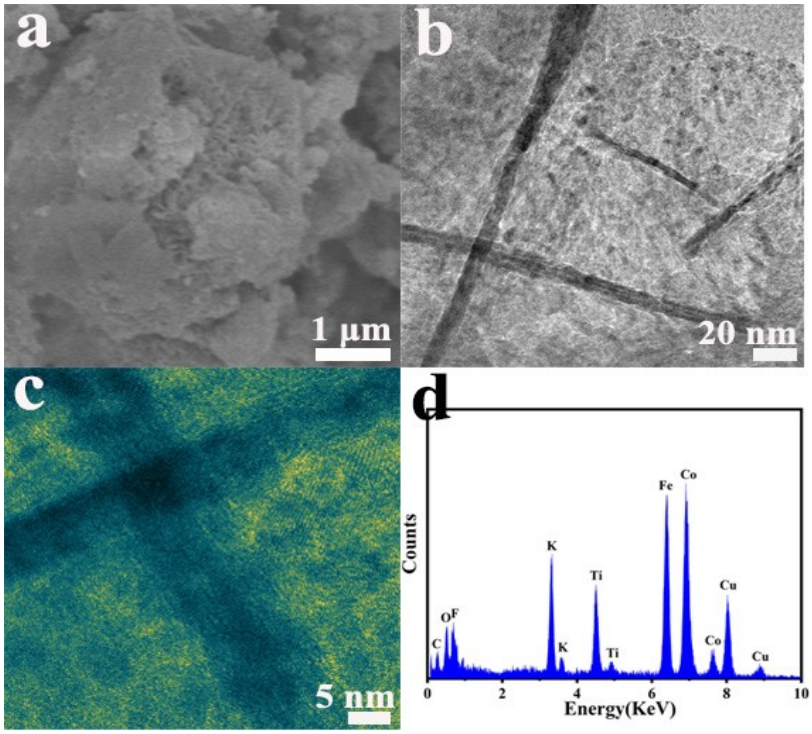

Fig. S7. (a) SEM images. (b)TEM images. (c) HRTEM images. (d) EDX spectra of CoF_2/FeF_2@MXene after electrochemical testing.

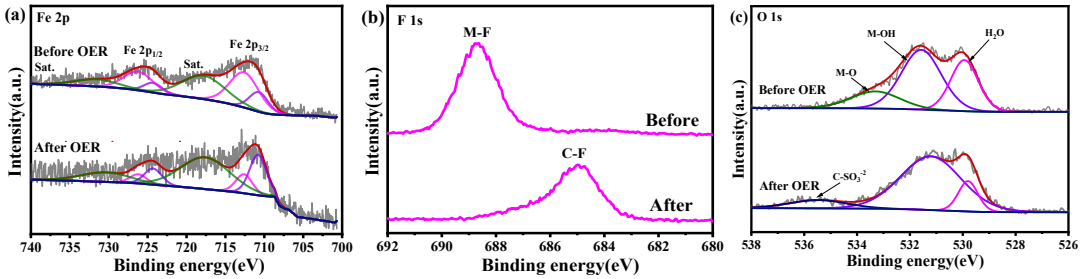

Fig. S8. High-resolution XPS spectrum for (a)Fe 2p; (b) F 1s and (c) O 1s before and after the OER test for CoF_2/FeF_2@MXene.

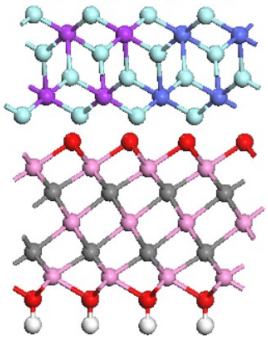

Fig. S9. The model of CoF_2/FeF_2@Mxene

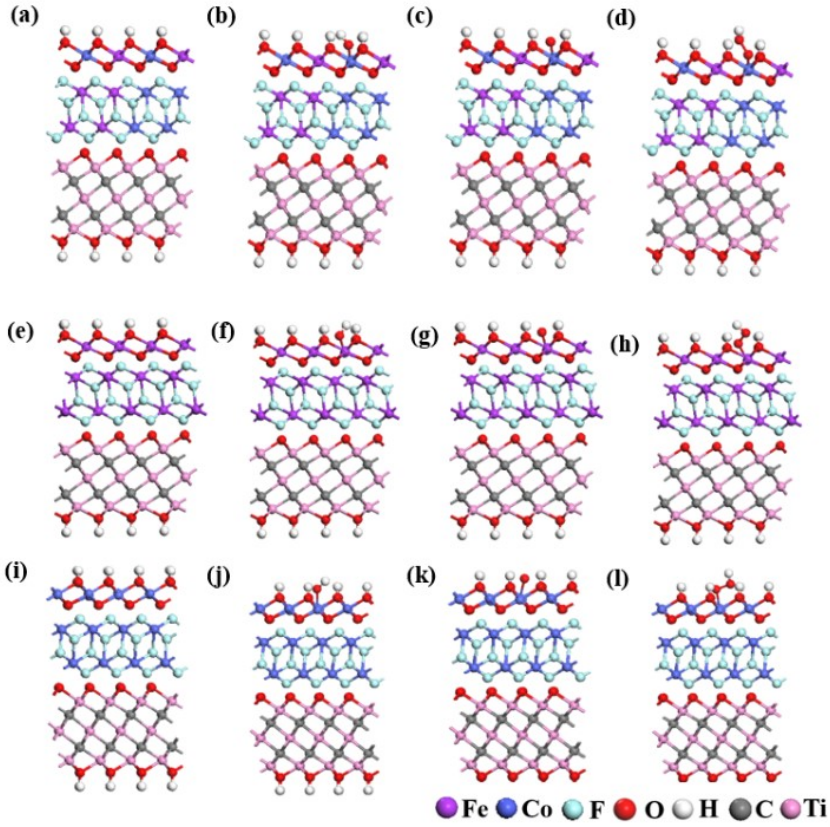

Fig. S10. A model for the adsorption of reaction intermediates on (a-d) CoF_2/FeF_2@Mxene, (e-h)

FeF_2/MXene and (i-l) FeF_2/Mxene surfaces.

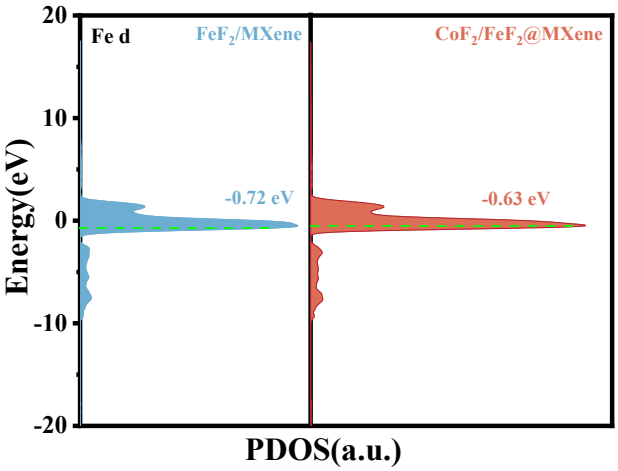

Fig.S11. PDOS of Fe d for FeF_2/MXene and CoF_2/FeF_2@MXene.

Table S1 The detailed binding energy of Co elements for CoF_2/FeF_2@MXene and CoF_2/MXene.

Catalysts	Co $2p_{3/2}$		Co $2p_{1/2}$		Relative content/%
	Peak	Binding energy/eV	Peak	Binding energy/eV	
CoF_2/FeF_2@MXene	Co-O	781.5	Co-O	797.8	19.7%
	Co-F	783.3	Co-F	799.6	80.3%
CoF_2/MXene	Co-O	781.5	Co-O	797.8	11.0%
	Co-F	783.3	Co-F	799.6	89.0%

Table S2. The detailed binding energy of Fe elements for CoF_2/FeF_2@MXene and FeF_2/MXene.

Catalysts	Fe $2p_{3/2}$		Fe $2p_{1/2}$		Relative content/%
	Peak	Binding energy/eV	Peak	Binding energy/eV	
CoF_2/FeF_2@MXene	Fe-F	712.6	Fe-F	726.2	74.0%
	Fe-O	710.7	Fe-O	724.3	26.0%
FeF_2/MXene	Fe-F	712.3	Fe-F	725.9	71.7%
	Fe-O	710.6	Fe-O	724.2	28.3%

Table S3. The comparison of some representative OER electrocatalysts in alkaline electrolyte.

Materials	Elecrode substrate	Overpotential (mV) @ 10 mA cm^{-2}	R_f
CoF_2/FeF_2@MXene	GCE	230	This work
MXene@CoS/FeS_2	GCE	278	[9]
NiSe–NiO/$Ta_4C_3T_x$ MXene	GCE	255	[10]
NiO-Ni_3Se_4/MXene	GCE	260	[11]
Ni/NiO_{150}	GCE	280	[12]
Ag/CoMo-LDH	GCE	290	[13]
FeNi LDH/$FeNi_2S_4$	GCE	259	[14]
$CoFe_2O_4$/β-$Ni(OH)_2$	GCE	278	[15]
CoOx/FeOx/CNTs	GCE	308	[16]
Co/CoS_2	GCE	349	[17]
MXene@TiO_2/FeP	nickel foam	240	[18]
NU-1000/$CuCo_2S_4$	nickel foam	335	[19]
$Fe_2O_3/ZnCo_2O_4$	nickel foam	261	[20]
$Co(CO_3)_{0.5}OH$/Cu	nickel foam	253	[21]
CoNiLDH/FeOOH	nickel foam	250	[22]
Co_2Ni-MOF@MX-1	carbon paper	265	[23]
FeS/Co_3S_4	carbon cloth	252	[24]
$NiSe_2/FeSe_2$	carbon cloth	256	[25]
CoFe-Co_xN@NC	carbon cloth	270	[26]
$Ni(OH)_2$/g-C_3N_4	platinum plate	240	[27]

Table S4. EIS fitting parameters from equivalent circuits for CoF_2/FeF_2@MXene, CoF_2/MXene and FeF_2/MXene samples in 1 M KOH.

Samples	R_s/Ω	R_{ct}/Ω	R_0/Ω	CHI/S s^{-n}
CoF_2/FeF_2@MXene	8.1	12.8	3.9	5.921e-05
CoF_2/MXene	7.1	50.2	1.2	2.901e-05
FeF_2/MXene	7.5	85.3	5.0	2.561e-05

Table S5. C_{dl}, ECSA and R_f for all samples.

Catalysts	C_{dl} (mF cm^{-2})	ECSA (cm^2)	R_f
CoF_2/FeF_2@MXene	2.0	3.5	50.0
CoF_2/MXene	0.84	1.47	21.0
FeF_2/MXene	0.75	1.31	18.75

Table S6. The detailed binding energy of Co elements for CoF_2/FeF_2@MXene before and after the durability test.

Catalysts	Co $2p_{3/2}$		Co $2p_{1/2}$		Relative content/%
	Peak	Binding energy/eV	Peak	Binding energy/eV	
CoF_2/FeF_2@MXene (Before OER)	C-O	781.5	C-O	797.8	19.7%
	Co-F	783.6	Co-F	799.9	80.3%
CoF_2/FeF_2@MXene (After OER)	Co-O	780.5	Co-O	796.8	100%

Table S7. The detailed binding energy of Fe elements for CoF_2/FeF_2@MXene before and after the durability test.

Catalysts	Fe $2p_{3/2}$		Fe $2p_{1/2}$		Relative content/%
	Peak	Binding energy/eV	Peak	Binding energy/eV	
CoF_2/FeF_2@MXene (Before OER)	Fe-O	710.7	Fe-O	724.3	26.0%
	Fe-F	712.6	Fe-F	726.2	74.0%
CoF_2/FeF_2@MXene (After OER)	Fe-O	710.9	Fe-O	724.5	100.0%

References:

1. J. Chun, C. Jo, S. Sahgong, M. G. Kim, E. Lim, D. H. Kim, J. Hwang, E. Kang, K. A. Ryu, Y. S. Jung, Y. Kim and J. Lee, *ACS Applied Materials & Interfaces*, 2016, **8**, 35180-35190.
2. X.-G. Zhang, P. Guo, J.-F. Han and K.-Y. Ye, *Chem. Commun.*, 2020, **56**, 8512-8523.
3. M. Pietrowski, M. Zieliński, E. Alwin, A. Suchora and J. Gawarecka, *RSC Adv.*, 2019, **9**, 5711-5721.
4. X. Gu, Z. Liu, M. Li, J. Tian and L. Feng, *Appl. Catal., B*, 2021, **297**, 120462.
5. X. Gu, Z. Liu, H. Liu, C. Pei and L. Feng, *Chem. Eng. J.*, 2021, **403**, 126371.
6. Y. Feng, S. Lu, L. Fu, F. Yang and L. Feng, *Chem. Sci.*, 2024, **15**, 2123-2132.
7. D. Vanderbilt, *Physical Review B*, 1990, **41**, 7892-7895.
8. J. Xu, L. Yu, B. Dong, F. Yang and L. Feng, *J. Colloid Interface Sci.*, 2023, **654**.
9. Z. Zhang, T. Liang, C. Jin, S. Zhang, Y. Cui, J. Chen and X. Zeng, *J. Mater. Chem. A.*, 2024, **12**, 14517-14530.
10. L. Yan, J. Liang and H. Li, *Int. J. Hydrogen Energy.*, 2023, **48**, 13159-13169.
11. L. Yan, J. Liang, D. Song, X. Li and H. Li, *Adv. Funct. Mater.*, 2024, **34**, 2308345.
12. Y. Liu, Z. Liu, L. Jia, D. Gao and Z. Tang, *Appl. Surf. Sci.*, 2022, **606**, 154897.
13. X.-Z. Song, J.-C. Ni, X.-B. Wang, J.-H. Dong, H.-J. Liang, Y. Pan, Y. Dai, Z. Tan and X.-F. Wang, *Inorg. Chem.*, 2023, **62**, 13328-13337.
14. J. Yuan, B. Huang, Y. Lu, H. Xu, Y. Qiao, H. Xu, G. He and H. Chen, *Appl. Surf. Sci.*, 2023, **610**, 155480.
15. K. Min, M. Kim, C. Lim, S. E. Shim, D. Lim and S.-H. Baeck, *Int. J. Hydrogen Energy.*, 2021, **46**, 27874-27882.
16. X. Yang, X. Sun, L.-Y. Gan, L. Sun, H. Mi, P. Zhang, X. Ren and Y. Li, *J. Mater. Chem. A.*, 2020, **8**, 15140-15147.
17. G. Gao, B. Fang, Z. Ding, W. Dong, Y.-X. Li, X. L. Wang and Y.-F. Yao, *Int. J. Hydrogen Energy.*, 2023, **48**, 1831-1841.
18. H. Su, X. Zeng, L. Gui, H. Zhao and X. Zhang, *J. Mater. Chem. A.*, 2025, **13**, 17042-17053.
19. S. Sanati, A. Morsali and H. García, *Int. J. Hydrogen Energy.*, 2023, **48**, 14749-14762.
20. S. Fu, Y. Ma, X. Yang, X. Yao, Z. Jiao, L. Cheng and P. Zhao, *Appl. Catal. B Environ.*, 2023, **333**, 122813.
21. X. Liao, T. Zhang, M. Dai, W. Yuan and H. Lin, *J. Alloys Compd.*, 2023, **936**, 168303.
22. P. Zhao, S. Fu, Y. Luo, C. Peng, L. Cheng and Z. Jiao, *Small*, 2023, **19**, 2305241.
23. P. Tan, R. Gao, Y. Zhang, N. Han, Y. Jiang, M. Xu, S.-J. Bao and X. Zhang, *J. Colloid Interface Sci.*, 2023, **630**, 363-371.
24. S. Deng, X. Zhang, Y. Zhang, J. Ye, B. Mei and S. Lin, *Int. J. Hydrogen Energy.*, 2024, **51**, 550-557.
25. S. Ni, H. Qu, Z. Xu, X. Zhu, H. Xing, L. Wang, J. Yu, H. Liu, C. Chen and L. Yang, *Appl. Catal., B.*, 2021, **299**, 120638.
26. X. Lin, J. Liu, L. Wu, L. Chen, Y. Qi, Z. Qiu, S. Sun, H. Dong, X. Qiu and Y. Qin, *AIChE J.*, 2022, **68**, e17785.
27. T. Li, X. Ma, J. Wu, F. Chu, L. Qiao, Y. Song, M. Wu, J. Lin, L. Peng and Z. Chen, *Electrochim. Acta.*, 2021, **400**, 139473.